MATERIALS SCIENCE

Programming angiogenesis with tunable assemblies of multifunctional peptides

Joseph Dodd-o[1,2], Bobak Shadpoor[1], Abhishek Roy[1], Roya Jafari[3], Tarunya R. Sudarshan[4], Abigail Holberton[5,6], Dongjing He[4,5], Francesco Coppola[3], Daniel M. Dinakarapandian[4], Deep Malu[4,5], Gelavizh Gharati[2], Alexandra Griffith[2], Harrison Rohe-Weiner[2], Siya Patel[2], Edward Bonder[7], Yuhang Hu[4,5], Levi Wood[5,6,8], Anant K. Paravastu[4,6], Petr Kral[3,9], Vivek A. Kumar[1,10,11,12,13]*

Therapeutic angiogenesis is constrained by the inability to localize, sustain, and finely tune vascular signaling. Here, we detail a supramolecular peptide system that enables angiogenic programming by decoupling mechanical integrity from receptor-level bioactivity. We integrate a vascular endothelial growth factor (VEGF)–mimetic amphiphile (SLan) with a mechanically robust β sheet peptide (K1) to yield injectable nanofiber hydrogels with tunable stiffness (100 to 1000 pascals) and preserved vascular endothelial growth factor receptor 2 (VEGFR2) affinity. Molecular dynamics simulations and solid-state nuclear magnetic resonance revealed that the coassembly mitigates steric interference between domains, enabling dense supramolecular packing while maintaining optimal receptor accessibility. The resulting SLan-K1 formulation preserves the secondary structure, activating canonical VEGFR2–MEK (mitogen-activated protein kinase kinase)–ERK (extracellular signal–regulated kinase). In vitro, these hydrogels induce endothelial proliferation; in vivo, they drive rapid neovascular infiltration and stable vascular integration in murine and rodent implants. This design unites peptide self-assembly, receptor binding kinetics, and immunophenotypic outcomes in defining a molecular framework for tunable angiogenic materials. This strategy establishes a modular platform for engineering instructive microenvironments that bridge molecular design and tissue-scale functionality.

INTRODUCTION

Therapeutic angiogenesis remains one of the grand challenges in regenerative medicine. The controlled regeneration of functional microvasculature underpins the recovery of ischemic tissues, the integration of engineered grafts, and the repair of chronic wounds. Yet, despite decades of clinical and preclinical effort, no off-the-shelf strategy has reliably reconstituted microcirculatory networks in vivo. Clinically approved growth factor delivery (e.g., becaplermin) has limited clinical acceptance due to concerns of off-target side effects (tumorigenicity/persistence of the growth factor in circulation) (*1*–*3*). Gene [e.g., hypoxia-inducible factor 1α (HIF-1α) transcription stimulation], RNA (e.g., long noncoding RNA GAS5), and stem cell (e.g., bone marrow–derived stem cells and engineered adipose-derived stem cells) have been attempted clinically with limited phase 2 trial success owing to localization, stability, and viability of delivered biologics, let alone concerns with multiple procedures and scale-up/age/culture times, especially with cell products (*1*, *4*–*7*). This highlights a gap in the design of an off-the-shelf scalable therapeutic that can be delivered to promote robust in situ angiogenesis for therapeutic revascularization.

The extracellular matrix (ECM) provides a template for how mechanical scaffolding and nanoscale biochemical signaling are integrated. Native ECM provides structural support and presents growth factors and receptor-binding ligands at the nanoscale, functions that are difficult to fully recapitulate with recombinant proteins or polymer carriers. Synthetic analogs that capture this duality could fundamentally shift therapeutic design. Supramolecular peptide assemblies can offer a modular bottom-up route toward such ECM mimetics. These short, rationally designed peptides self-assemble into nanofibrous hydrogels that are injectable, biodegradable, and highly tunable in stiffness and bioactivity. Their dynamic noncovalent interactions enable self-healing and controlled degradation, whereas their sequence programmability allows the integration of growth factor–mimetic motifs directly into the self-assembling backbone. However, incorporating bulky bioactive domains often disrupts the β sheet architecture that governs fibrillization, leading to weak gels and reduced receptor accessibility. This intrinsic trade-off between mechanical integrity and molecular bioactivity remains a central unsolved problem.

We published the description of a self-assembling peptide (SAP) that contains a mimic of vascular endothelial growth factor A (VEGF-A) (termed QK) (*8*, *9*). This peptide showed remarkable local in vitro and in vivo angiogenesis compared to other SAPs, as well as therapeutic benefit in treating murine hindlimb ischemia (*10*). Briefly, the peptide termed SLanc has a β sheet self-assembling backbone

[1]Department of Biomedical Engineering, University of Houston, Houston, TX 77204, USA. [2]Department of Biomedical Engineering, New Jersey Institute of Technology, Newark, NJ 07102, USA. [3]Department of Chemistry, University of Illinois at Chicago, Chicago, IL 60607, USA. [4]School of Chemical and Biomolecular Engineering, Georgia Institute of Technology, Atlanta, GA 30332, USA. [5]George W. Woodruff School of Mechanical Engineering, Georgia Institute of Technology, Atlanta, GA 30332 USA. [6]Parker H. Petit Institute for Bioengineering and Biosciences, Georgia Institute of Technology, Atlanta, GA 30332, USA. [7]Department of Biological Sciences, Rutgers University, Newark, NJ 07102, USA. [8]Wallace H. Coulter Department of Biomedical Engineering, Georgia Institute of Technology, Atlanta, GA 30332, USA. [9]Departments of Physics, Pharmaceutical Sciences, and Chemical Engineering, University of Illinois at Chicago, Chicago, IL 60607, USA. [10]Department of Health Systems and Population Health Sciences, UH College of Medicine, University of Houston, Houston, TX 77204, USA. [11]Texas Institute of Measurements and Statistics (TIMES), University of Houston, Houston, TX 77204, USA. [12]UH Drug Discovery Institute, University of Houston, Houston, TX 77204, USA. [13]William A. Brookshire Department of Chemical and Biomolecular Engineering, University of Houston, Houston, TX 77204, USA.
*Corresponding author. Email: vkumar24@cougarnet.uh.edu

(K-SLSLS"L-RG"-SLSLSL-K), with a central "LRG" forming a matrix metalloproteinase (MMP) cleavable scissile bond enhancing in vivo biodegradation, a single glycine spacer, and an appended mimic of VEGF-A (termed QK: KLTWQELYQLKYKGI), SLanc sequence K-SLSLSL-RG-SLSLSL-K-G-KLTWQELYQLKYKGI (*8*, *11*, *12*). These injectable SAP boluses of SLanc rapidly infiltrated in vivo with cells that deposit native niche-specific tissue are metabolized in situ and rapidly excreted if they enter circulation, negating the concerns related to full growth factor persistence and off-target side effects. Combined, these features present an opportunity to both localize and extend the therapeutic window of the multidomain peptide (MDP). Despite promise in small animal models, subsequent work with SLanc revealed that its poor mechanical/gelation properties ($G' < 100$ Pa) relegated its use for short-term angiogenesis with poor long-term outcomes, especially in larger animal models. Addressing degradation and mechanical strength (partially), by improving supramolecular packing, we engineered SLan (sequence K-SLSLSLSLSLSL-K-G-KLTWQELYQLKYKGI) (without the LRG scissile bond) that was able to promote longer-term vascularized regeneration of tissue in vitro and in a large animal (canine) pulp regeneration model (*13*). A prior work from our group revealed that increased uniform SAP monomer density results in obfuscation and steric blocking of appended mimetic sequences, which may adversely affect target binding (*14*).

Several SAP platforms have been explored for therapeutic angiogenesis from modified peptide amphiphile (PA) nanofibers, MDP hydrogels, RADA16-based hydrogels, and composite MDP-liposome systems (*15*–*18*). Although demonstrating angiogenic efficacy, mechanical properties and bioactive signaling are intrinsically coupled in these systems. In PA-QK systems, increasing epitope density simultaneously alters nanofiber stiffness and packing. In RADA16 and MDP systems, angiogenesis relies on exogenous growth factor loading or innate material-host interactions rather than on rationally designed receptor-mimetic domains (*17*). A recent comprehensive review catalogs these and additional SAP-based angiogenic strategies, again highlighting the unmet need for systems that decouple bioactivity and mechanical/structural property trade-offs (*19*).

To balance this trade-off, we reasoned that structural and bioactive roles must be distributed across complementary monomers. Here, we introduce a coassembling peptide platform that unites a mechanically robust, unfunctionalized β sheet peptide (K1: K-SLSLSLSLSLSL-K) with the bioactive VEGF-mimetic SLan to form hybrid nanofibers. The SLan-K1 coassembly strategy addresses the mechanical properties limitation by distributing structural (K1) and bioactive (SLan) functions across complementary monomers within the same supramolecular lattice. By simply adjusting the SLan:K1 molar ratio, we engineer to improve mechanical properties while conserving or improving vascular endothelial growth factor receptor 2 (VEGFR2) binding affinity—a degree of modularity not achievable in single-component systems. Molecular dynamics (MD) simulations and solid-state nuclear magnetic resonance (NMR) demonstrated that K1 coassembly can mitigate steric congestion within SLan fibrils while preserving both supramolecular order and VEGFR2 accessibility. The resulting 1:1 formulation activates canonical VEGFR2–mitogen-activated protein kinase (MAPK) kinase (MEK)–extracellular signal–regulated kinase (ERK) signaling comparable to VEGF-A, elicits robust endothelial infiltration, and promotes stable neovascularization in vivo without exogenous growth factors.

By integrating computational modeling, receptor-level kinetics, and in vivo immunophenotyping, this study establishes a molecular design framework for programmable angiogenic scaffolds. Beyond angiogenesis, the principles uncovered here—decoupling bioactivity from mechanics through supramolecular partitioning—provide a blueprint for synthetic morphogen systems capable of orchestrating complex tissue regeneration.

RESULTS AND DISCUSSION

Bioactive region interference in fibril self-assembly

For spontaneously self-assembling thixotropic materials such as SAPs, the assembly into fibrils, which are long enough to entangle, allows for the formation of a "stiff" (storage modulus ranging from 10 to 1000 Pa) gel structure. We have long hypothesized the assembly of monodomain SAPs into antiparallel β sheets and observed slight energetic favorability in this conformation in silico (fig. S1), complementing previous studies that established the presence of antiparallel β sheets analyzed in bulk by circular dichroism (CD) or Fourier transform infrared resonance (FTIR) spectroscopy (*8*, *12*, *14*, *20*, *21*). Although still thixotropic and forming shape-holding gels under low shear conditions, SLan has a measurably lower storage modulus compared to K1 owing to the bulky QK bioactive domain of the peptide hindering β sheet packing and self-assembly into fibers (Fig. 1) (*10*, *13*).

MD simulations of the formation of fibrils demonstrated that the QK domain interferes with the initial nucleation of the fibril. In the K1 simulation, randomly dispersed monomers spontaneously assembled into a β sheet with close interactions of the amphiphilic domain (-SL-) leucine residues (Fig. 1A). Conversely, MD simulations revealed that SLan's QK region is frequently inserted into the supramolecular self-assembling β sheet, amphiphilic (-SL-) regions, interrupting the leucine alignment that forms the β sheet structure (Fig. 1C). A randomly dispersed 1:1 combination of SLan and K1 monomers appeared to reverse this phenomenon, allowing for spontaneous leucine alignment akin to K1 (Fig. 1B). Additional MD investigations into fibril assembly demonstrated similar patterns, with K1 monomers docking and elongating the fibril (Fig. 1D), and the QK region of SLan interfering with the leucine-mediated docking and elongation (Fig. 1F). Similar to the nucleation simulations (Fig. 1, A and B), the 1:1 combination demonstrated evidence of docking along the leading edge like K1, suggesting a recapitulation of assembly kinetics missing from pure SLan (Fig. 1E). The assembled fibrils remained stable during the course of simulations (Fig. 1, G to I). QK assembly's impedance modeled in silico was supported by congruent observations of shorter fibrils of SLan compared to K1 in atomic force microscopy (AFM) (Fig. 1, J and L). Cryo–electron microscopy (cryo-EM) of hydrogels confirmed these observations (without potential AFM drying artifact) with a pattern of decreasing fibril length and increasing relative SLan concentration (Fig. 1, M and O, and figs. S2 to S4). As the length of fibrils shorten, the probability of contact among the fibrils is consequently decreased, leading to fewer entanglements, and a consequent lower stiffness of the supramolecular polymeric network. This matched our macroscopic observations in oscillatory rheometric analysis, with an ~10-fold reduction in low-strain storage modulus of SLan compared to K1 (Fig. 1, P and R). We believe that the progressive decrease in fibril length with increasing SLan proportion (Fig. 1, J to O) affects angiogenic function by reducing interfiber contact and entanglement, yielding softer gels (Fig. 1, P to R) that degrade more rapidly in vivo. The 1:1 coassembly partially recovers both fibril length and mechanical integrity (Fig. 1, K, N, and Q), bridging material-level observations

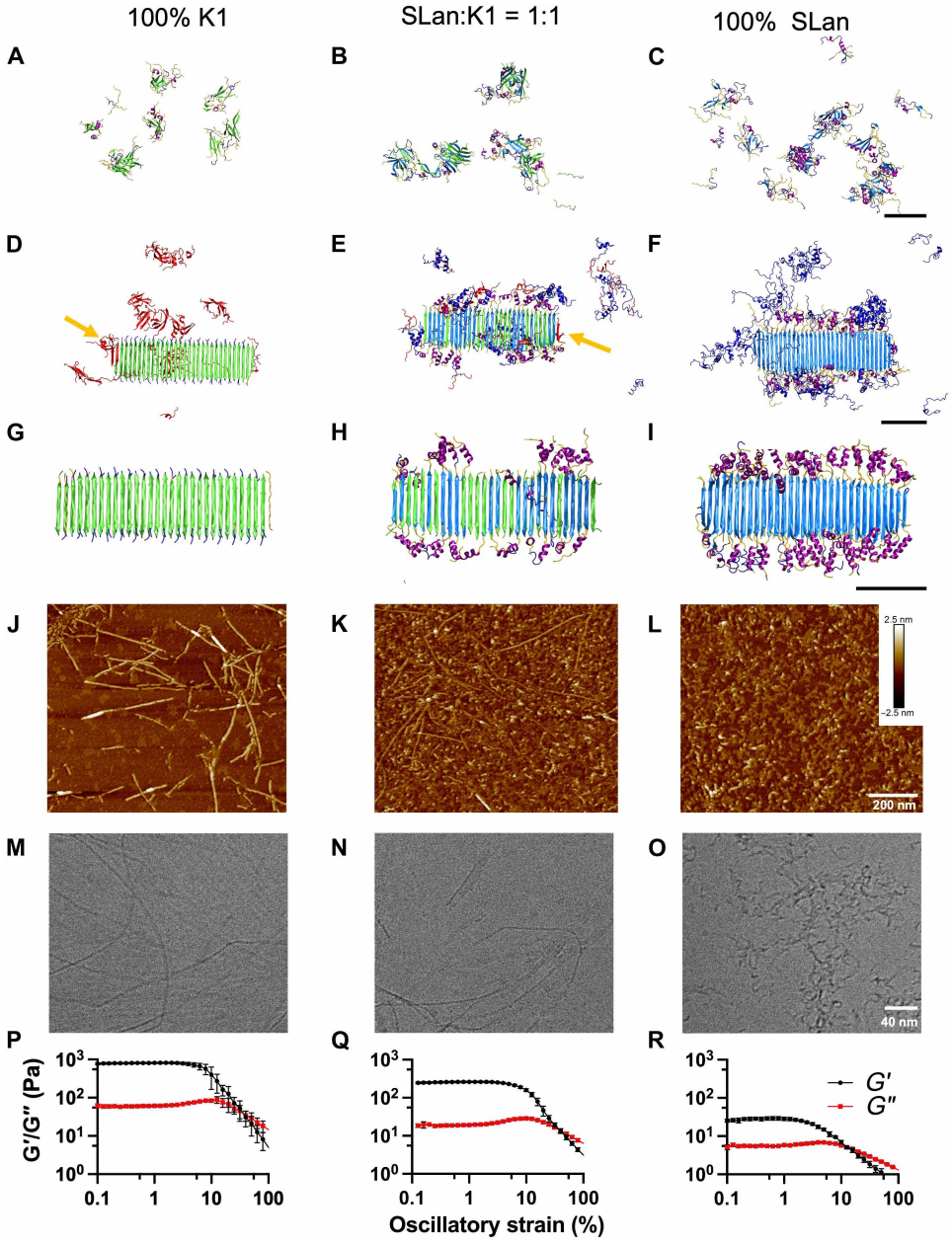

Fig. 1. Fiber assembly of homogeneous and composite peptide hydrogels. (**A**) Simulation interrogating K1's ability to self-assemble into β sheets showed spontaneous β sheet assembly, consistent with previous in vitro investigations into the structure. (**B**) This phenomenon was recapitulated for 50:50 (mol/mol) combinations of SLan (blue/purple) and K1 (green/orange), whereas the α-helical bioactive domain (purple) appears to start interfering with the structure. (**C**) This interference becomes more pronounced with SLan as the α helix starts interfering more prominently. (**D**) Fiber elongation studies show spontaneous docking of K1 monomers (orange) against the K1 fiber. (**E**) 1:1 SLan:K1 combinations show arrangement against the fiber with increased difficulty finding the binding pocket. (**F**) The α helix interference of docking against the fibril is even more prominent for 100% SLan. (**G** to **I**) Full fiber simulations of K1, 1:1 SLan:K1, and SLan in the hypothesized β sheet self-assembled structure. Although we noticed interactions between the α-helical QK regions, the structures did not disassemble after 1 μs of simulation. (**J**) AFM of K1 on mica showing linear β sheet fibrillar assemblies. (**K**) These assemblies become smaller and more variable in length as SLan is added. (**L**) 100% SLan has consistently smaller fibrils, leading to less entanglement and interfiber interactions. (**M** to **O**) This pattern was further substantiated with examinations of the fiber morphology under cryo-EM, showing progressively less orderly fiber formation with proportionally more SLan. (**P** to **R**) Consistent with the observed smaller fibrils, we see a progressive decrease in the low-strain rate storage modulus (black line) with increasing SLan.

to that observed in vivo, including comparable endothelial cell recruitment and neovascularization to SLan alone.

Enhancing stiffness with combination peptide hydrogels

Following the observations of the pure K1 and SLan fibrils, we combined the two peptides in molar ratios of 9:1, 3:1, 1:1, 1:3, and 1:9 SLan:K1. We saw that the combination SAPHs have a direct relationship between storage moduli (in the gel regime at low strain) and the K1 ratio (Fig. 1Q and figs. S5, O to R, and S6), corroborated by AFM fibril length (Fig. 1K and fig. S5, G to J) and cryo-EM fibril length and morphology (Fig. 1N and fig. S5, K to M). Evidence of K1 assisting assembly was supported by MD simulations of the hypothesized coassembled fibers. In the monomer assembly simulations, the 1:1 combination was able to recapitulate the leucine alignment of pure K1 (Fig. 1B). Higher SLan doping (e.g., 1:3 and 1:9 K1:SLan monomer assemblies) show QK interfering with leucine alignment, getting more pronounced with higher SLan concentration (fig. S5, A and B).

CD and solid-state NMR spectroscopy indicate that K1 domains alone [K-$(SL)_6$-K] and within SLan peptides [(K-$(SL)_6$-K)-GKLTWQELYQLKYKGI] predominantly assembled into β sheets and that the angiogenic domain is solvent accessible (Fig. 2A). CD

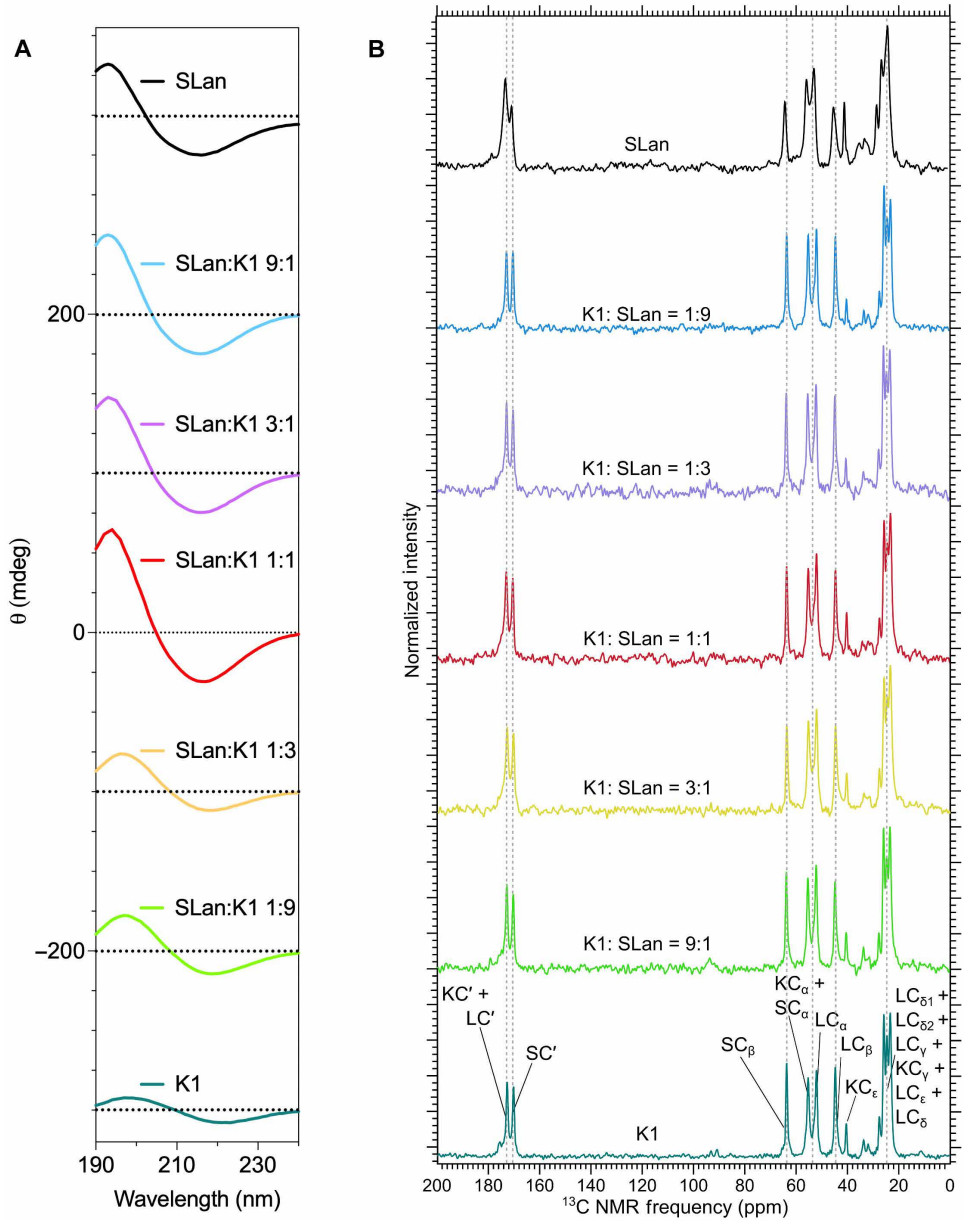

Fig. 2. Structural Investigation of combination assemblies. (**A**) CD of SLan, K1, and combinations show indications of the residual α helix in SLan, with the peak/trough progressively moving toward 220 nm with more K1. (**B**) ^{13}C CP/MAS solid-state NMR of combinations show consistent ordered β sheet assembly regardless of combinations, substantiating the CD data at the inter/intramolecular scale and supporting conservation of the β sheet self-assembly motifs. Detailed assignments show common features for K1, SLan, and combinations.

spectroscopy exhibit characteristic β sheet minima at 220 nm for K1, SLan, and for all molar ratios of SLan:K1 coassembly, largely conserved for the combinations of SLan and K1 (Fig. 2). The NMR spectra were generated using ^{1}H-^{13}C cross-polarization/magic angle spinning (CP/MAS) solid-state NMR measurements (*22*), which selects for atoms in rigid (e.g., β sheet domains) over flexible solvent-accessible domains (Fig. 2B). These NMR spectra were labeled using partial assignments on carbon atoms on the residues in peptide K1 and all molar ratios of SLan:K1 using known chemical shift ranges for β sheets (*23*). All molar ratios of Slan:K1 and K1 NMR spectra exhibit S and L carbonyl (CO), α carbon (C_α), and β carbon (C_β) ^{13}C NMR chemical shifts consistent with β strand secondary structure (table S4) (*23*). All NMR spectra are highly ordered assemblies with linewidths below 1 part per million (ppm) comparable to highly ordered amyloids (table S4) (*24*–*26*). Furthermore, we compared these NMR spectra with that of pure SLan whose NMR spectra were analyzed from previous data collected (*20*). The amino acids in the angiogenic domain in the SLan peptide contribute little intensity to the signal even with large SLan/K1 ratios. Overall, the spectra (Fig. 2A) are all similar despite the variable presence of the angiogenic domain within the SLan peptide, indicating that the angiogenic domain is solvent accessible and dynamic and hence does not experience ^{1}H-^{13}C cross-polarization.

Maintaining affinity to the target receptor with combination peptide hydrogels

Functionalized SAPs are designed to bind to a specific receptor with a rationally designed bioactive domain and self-assemble with other multidomain monomers (*14*, *21*, *27*–*33*). To explore the designed interaction of the bioactive domain of the peptide with VEGFR2, we simulated two independent VEGFR2 proteins (Fig. 3, A to C, and fig. S7) both positioned on different fibers in a physiological solution and placed on opposite sides of the fibers, away from each other, and free to move along the fibers. The modeling of these interactions showed that there is a general conservation of binding energy up to a 1:1 combination of SLan and K1 (Fig. 3D and fig. S8), with K1 not showing appreciable binding to VEGFR2 (Fig. 3E).

In vitro spectral shift investigations into the binding affinity followed a similar pattern to MD simulations. K1 showed a low affinity to VEGFR2, with the calculated dissociation constant (K_d) being ~1 order of magnitude higher than in SLan (Fig. 3E and fig. S9), suggesting a nonspecific binding. Combinations of SLan and K1 revealed progressively higher affinity (lower K_d) with increasing SLan proportion from 0 to 50% (Fig. 3E), consistent with our hypothesis of a combination being able to conserve binding. Ratios of 50 to 0% SLan had progressively higher K_d. All experimental groups were formulated at the same total peptide molar concentrations, ensuring that observed differences reflect molecular compositional effects (i.e., SLan:K1 molar ratio) rather than dose-dependent responses. The 1:1 SLan:K1 group therefore contains half the molar concentration of SLan compared to the pure SLan group yet achieves comparable angiogenic outcomes. This, combined with the dose-dependent response of SLan (fig. S9), supports the hypothesis that coassembly enhances per-mole bioactive efficiency by mitigating steric interference and improving epitope accessibility.

MD simulations directly informed the experimental design in three key ways. First, the observation that the α-helical QK domain sterically inhibits β sheet packing (Fig. 1, C and F) predicted that pure SLan would form shorter fibrils with correspondingly weaker gel properties—a prediction validated by AFM (Fig. 1, J to L) and oscillatory rheology (Fig. 1, P to R). Second, coassembly simulations demonstrated that K1 monomers rescue leucine alignment (Fig. 1B), directly guiding our selection of the 1:1 ratio as the primary formulation for biological studies. Third, receptor binding energy calculations (Fig. 3D) predicted that VEGFR2 affinity would be conserved up to 50% K1 dilution, which was confirmed with in vitro spectral shift binding kinetics showing that K_d values plateau between 50 and 100% SLan (Fig. 3E). Thus, the computational framework served as a predictive framework that informed our hypothesis, validated in vitro.

Downstream VEGFR2 signaling activation

Recent works have established that the self-assembling domain alone can be bioactive and serve as an engineering tool for enhancing bioactivity in multidomain SAPHs (*34*–*36*). We note that differential VEGFR2 activation may experience rapid turnover/dephosphorylation resulting in challenges with direct detection and interpretation of receptor activation, despite biophysical binding demonstrated by MicroScale Thermophoresis (MST) (Fig. 3E). This warranted downstream receptor pathway interrogation to understand the durability and temporal effects of the signaling cascade.

We investigated VEGFR activation and ultimately endothelial cell activity in vitro and in vivo in the presence of a VEGFR inhibitor, axitinib. We first interrogated the downstream MAPK cascade by stimulating serum-starved human umbilical cord endothelial cells (HUVECs) with SLan and K1, along with combinations of 1:1 SLan and K1 (figs. S10 to S13). To ensure that the constructs also lead to canonical activation of VEGFR2, we performed a Luminex multiplexed immunoassay for the MAPK pathway.

We interrogated common downstream targets of VEGFR2: phosphorylated MEK1, ERK1/2, and signal transducer and activator of transcription 1 (STAT1). We observed differential phosphorylation of these proteins when cultured with SLan or the canonical ligand VEGF-A relative to the vehicle control (Fig. 3F). This was not observed to the same degree by K1. VEGF-A demonstrated ERK1/2 phosphorylation in the MAPK pathway at this time point, whereas the 1:1 ratio targeted MEK and ERK1/2 phosphorylation. VEGF-A activates MEK/ERK faster than 1:1 ratios, but the 1:1 ratio activates MEK/ERK significantly more than K1 and SLan alone (Fig. 3, F to H). Notably, the presence the VEGFR inhibitor axitinib showed a significant knockdown in downstream pMEK and pSTAT1 signaling (Fig. 3, G and H), indicating specificity. This supports the hypothesis that the pathway is directly bridging the observed affinity and angiogenic effects seen in vivo. Furthermore, the downstream signaling results are indicative of a delayed activation of the kinase cascade by the peptide combinations relative to VEGF-A. Future studies may further interrogate the temporal dynamics of activation and persistent signaling (*37*).

In vivo endothelial cell recruitment and neovascularization

To evaluate how supramolecular composition influences neovascular recruitment and matrix persistence, we examined subcutaneous hydrogel implants under normophysiologic conditions to avoid unique concomitant (ischemic) disease-specific pathophysiologic adaptations. Previous histologic investigations of SLan/SLanc have revealed rapid bolus cellular infiltration (days 1 to 3) and in situ specific neovascularization at 3 to 7 days (*13*, *34*, *38*). Explanted boluses at 3 and 7 days were digested and analyzed for cellular infiltrate

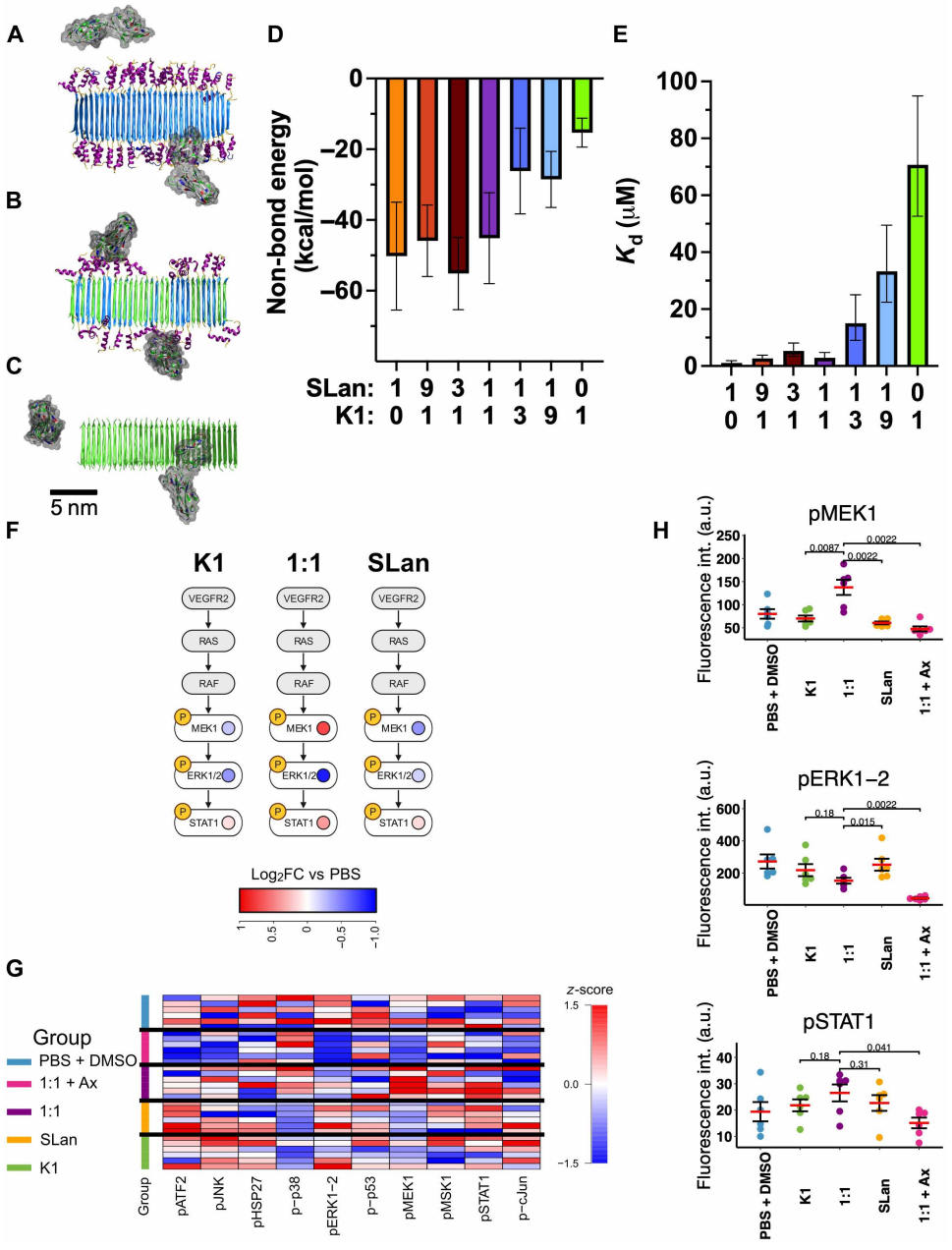

Fig. 3. Combination SLan/K1 hydrogels exhibit preserved receptor binding. MD investigations were performed on (**A**) 100% SLan, (**B**) 1:1 molar ratio of SLan and K1, (**C**) 100% K1. The 60-mer fibrils were assumed to be randomly coassembled (random distribution of SLan and K1 along the fibril). The simulations were performed in duplicate runs, with the binding energy of each VEGFR2 (of three receptors per run) calculated. (**D**) Investigations into the non–bond energy of each receptor showed increasing binding energy with increasing SLan concentration (average ± SEM). (**E**) This trend was conserved when we investigated that the binding affinity of the peptide combinations against VEGFR2. K1 (orange) had ~1 order of magnitude higher dissociation constant (K_d) compared to SLan, suggesting nonspecific binding of K1 to VEGFR2. The predicted dissociation constant is represented by the bars in the graph, with the calculated confidence interval represented as the bars. (**F**) Luminex assay was performed on HUVECs treated with our peptide combinations. We observed a similar degree of phosphorylation for kinase ERK1/2 and transcription factor STAT1 with all treatment groups. Conversely, we observed a drastic increase in MEK1 for the 1:1 combination. Scale is normalized to the PBS + DMSO control. FC, fold change. (**G**) Expanded heatmap of selected phosphoprotein biomarkers. Each row represents data from an individual treatment well, *z*-scored along each column. Ax, axitinib. (**H**) Fluorescence values for key signals within the canonical pathway. a.u., arbitrary units. Data are plotted as means ± SEM, and *P* values between groups were calculated using a Wilcoxon rank-sum test with a Bonferroni correction applied for multiple comparisons.

using flow cytometry. Flow cytometry analysis revealed a marked increase in both total ($CD31^+$) and mature endothelial ($CD31^+$/$CD144^+$/$VEGFR2^+$) cell infiltration in SLan relative to K1 (Fig. 4, A to C) (*39*, *40*). The 1:1 SLan:K1 formulation reproduced this pro-angiogenic phenotype, comparable levels of total and differentiated endothelial cells to SLan alone at day 3 (Fig. 4C). The magnitude of the effect size decreased by day 7, but no significant difference in endothelial cell recruitment was observed (Fig. 4C). Dimensional reduction via t-distributed Stochastic Neighbor Embedding (tSNE) mapping demonstrated that SLan and 1:1 combination scaffolds clustered within a shared endothelial phenotype space, whereas K1 samples localized to a distinct region characterized by diminished VEGFR2 expression (Fig. 4, D to G). This balance between bioactivity and mechanical persistence supports the concept that coassembly extends the therapeutic window of VEGF-mimetic signaling by preventing premature gel dissolution while maintaining receptor accessibility. These data suggest that introducing K1 does not attenuate SLan-driven receptor-mediated recruitment but instead stabilizes a mechanically robust matrix capable of sustaining the angiogenic response corroborated by histological studies.

Hematopoietic and immune cell dynamics

To dissect the accompanying immune dynamics, we profiled hematopoietic subpopulations by flow cytometry (Fig. 5 and figs. S14 to

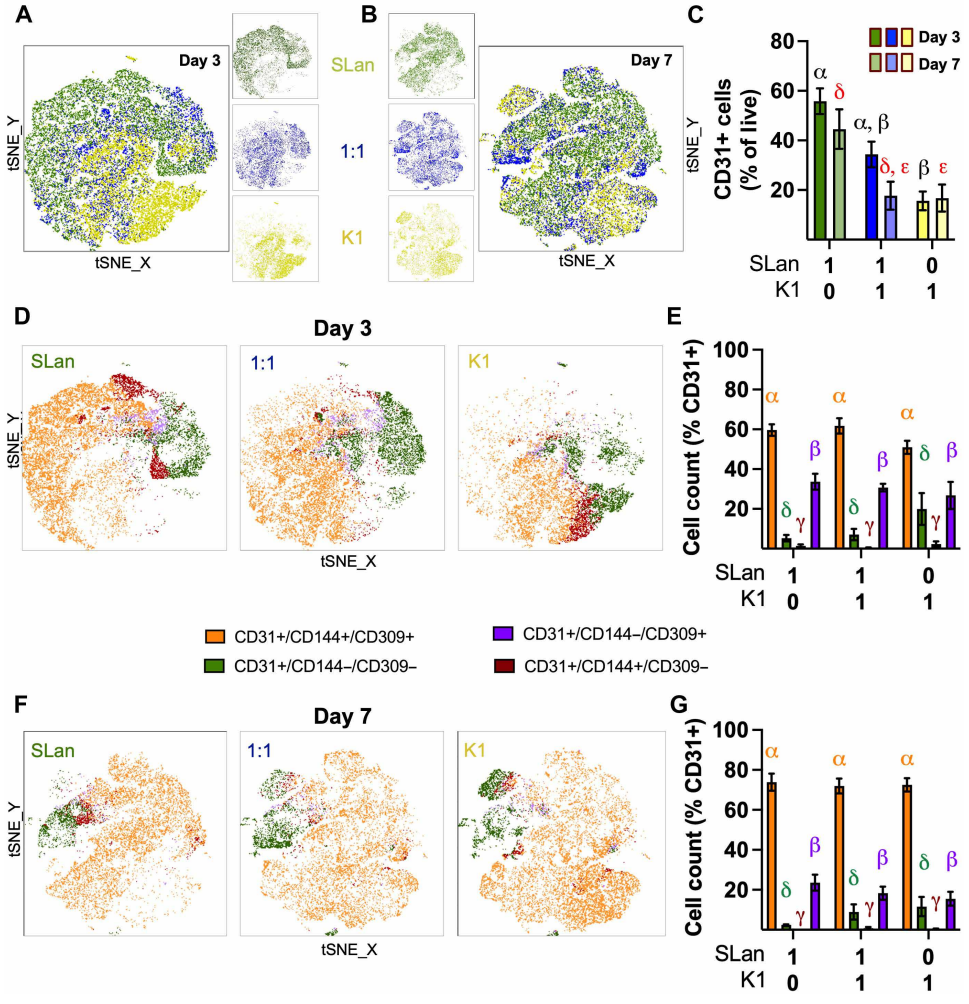

Fig. 4. Flow cytometry analysis of endothelial lineage cell infiltrates. tSNE clustering showing the relative distribution of cell populations among three test scaffolds (SLan, 1:1 combo, and K1) at (**A**) day 3 and (**B**) day 7. (**C**) Differential % live cells expressing $CD31^+$ cells that infiltrate the different hydrogels at days 3 and 7. One-way ANOVA revealed significant effect on day 3 $CD31^+$ cell infiltration [$F(2,12) = 17.91$, $F_{crit} = 3.89$, $P = 0.00025$, $\varepsilon^2 = 0.701$, $\eta^2 = 0.7882$, large effect]. Post hoc independent samples *t* tests with Bonferroni correction (adjusted $\alpha = 0.05/3 = 0.017$) revealed significant differences between K1 and SLan ($P = 0.00036$, Cohen's $d = 3.07$, large effect); other interactions were insignificant. One-way ANOVA revealed that hydrogel treatment had a significant effect on day 7 $CD31^+$ cell infiltration [$F(2,12) = 5.98$, $F_{crit} = 3.89$, $P = 0.0158$, $\varepsilon^2 = 0.416$, $\eta^2 = 0.499$, large effect]. Post hoc independent samples *t* tests with Bonferroni correction (adjusted $\alpha = 0.05/3 = 0.017$) revealed significant differences between K1 and SLan ($P = 0.00036$, Cohen's $d = 2.67$, large effect); other interactions were insignificant. (**D**) tSNE clustering of SLan, 1:1 combo, and K1 as a representation of the different endothelial cell populations at day 3. We noted that the 1:1 combination recapitulated the differentiated endothelial cell population (orange) on the left side of the TSNE *x* axis that is largely absent in K1. (**E**) Percentages of the different EC populations showing the diversity of marker expression by treatment group. (**F**) tSNE clustering of SLan, 1:1 combo, and K1 as a representation of the different endothelial cell populations at day 7. (**G**) Differential expression of $CD31^+$ endothelial cells using CD309 (VEGFR2) and CD144 (VE-Cadherin). Data are represented as means ± SEM. Significance between groups is represented by different Greek letters. All hydrogel treatments were sampled as $n = 5$.

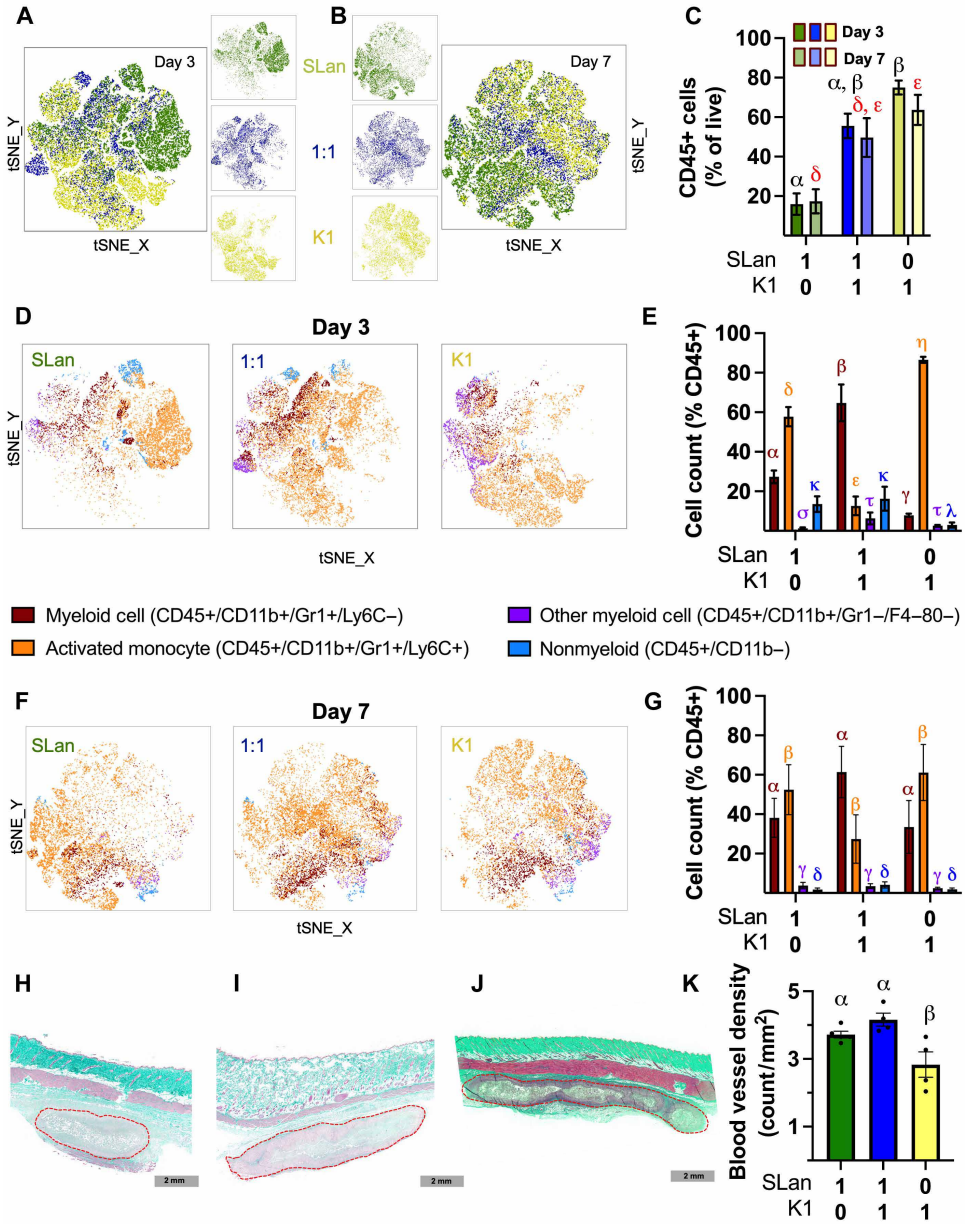

Fig. 5. Flow cytometry analysis of hematopoietic cell infiltrates. (**A**) tSNE clustering showing relative differences in cell population distribution among SLan, 1:1 combo, and K1 scaffolds. (**B**) % $CD45^+$ cells from live infiltrates and (**C**) myeloid ($CD45^+/CD11b^+$; dark) and nonmyeloid ($CD45^+/CD11b^-$; light) populations differ significantly across hydrogels. At day 3, hydrogel treatment significantly affected myeloid infiltrates [Kruskal-Wallis: $\chi^2(2) = 7.28$, $P = 0.026$, $\omega^2 = 0.44$]; post hoc Wilcoxon tests (Bonferroni-corrected $\alpha = 0.017$) revealed a significant difference between K1 and SLan only ($P = 0.016$, $r = 0.76$). At day 7, no significant effect on myeloid infiltrates was detected [one-way ANOVA: $F(2,12) = 1.52$, $P = 0.259$, $\eta^2 = 0.18$]. (**D**) tSNE clustering of myeloid subpopulations at day 7. (**E**) % cell subpopulations from $CD45^+$ infiltrates at day 3. Hydrogel treatment significantly affected Gr-1^+/Ly6C^- myeloid cells [ANOVA: $F(2,12) = 25.69$, $P < 0.001$, $\eta^2 = 0.81$] and activated monocytes [$CD45^+/CD11b^+$/Gr-1^+/Ly6C^+; ANOVA: $F(2,12) = 86.83$, $P < 0.001$, $\eta^2 = 0.94$], with all pairwise comparisons significant (Bonferroni-corrected t tests, all $P < 0.006$, Cohen's $d = 1.84$ to 9.40). Nonmyeloid infiltrates also differed significantly [Kruskal-Wallis: $\chi^2(2) = 7.44$, $P = 0.024$, $\omega^2 = 0.43$]; K1 versus SLan was the only significant pairwise difference (Wilcoxon, $P = 0.016$, $r = 0.66$). (**F** and **G**) tSNE clustering and $CD45^+$ phenotypic proportions show no significant differences at day 7. Data are represented as means ± SEM; significance denoted by Greek letters. (**H** to **J**) Masson's trichrome staining shows collagen deposition and vessel formation in (H) SLan, (I) K1, and the (J) 1:1 combination by day 7. (**K**) Treatment significantly affected blood vessel density [ANOVA: $F(2,10) = 7.85$, $P = 0.009$); post hoc comparisons (Holm's correction) showed higher density in SLan versus K1 ($P = 0.043$, $d = 1.70$) and 1:1 combo versus K1 ($P = 0.009$, $d = 2.22$).

S17). The K1 group exhibited elevated infiltration of total $CD45^+$/$CD11b^+$ myeloid cells compared to SLan (Fig. 5C), reflecting enhanced early myeloid recruitment within stiffer matrices containing K1. The 1:1 combination treatment group did not reveal significant differences in $CD45^+$/$CD11b^+$ cell recruitment from SLan or K1 at days 3 and 7 (Fig. 5C). Phenotypic subdivision revealed that 1:1 hydrogels contained a greater fraction of Gr-1^+/Ly6C^- myeloid cells and fewer activated monocytes (Ly6C^+) than either parent peptide (Fig. 5E). Because Ly6C^+ monocytes are associated with early phagocytic clearance whereas Gr-1^+/Ly6C^- myeloid cells contribute to immune resolution and vascular maturation, this shift may imply that 1:1 coassemblies accelerate the transition from inflammatory to reparative phases (*41*–*43*). By day 7, immune composition converged across groups, indicating that the initial differences primarily govern early microenvironmental conditioning rather than terminal inflammation (Fig. 5G). Notably, K1 retained a higher proportion of activated monocytes (Ly6C^+) relative to Gr-1^+/Ly6C^- myeloid cells, suggestive of a delayed transition to a reconstructive niche (Fig. 5, E and G). Although our gating strategy uses Gr-1^+ (Ly6C/Ly6G) staining, a limitation of our gating approach is in the explicit differentiation of Ly6G^+ cells, eliminating our ability to differentiate neutrophils. Furthermore, markers of macrophage polarization were not examined in this particular study (*44*, *45*). Countering these limitations was the absence of a significant difference in the non–myeloid cell subpopulations at days 3 and 7 (Fig. 5 and fig. S15), allowing for future studies for more discrete phenotype analysis for the source of the other myeloid infiltrates in a chronic inflammatory state (*36*, *46*).

To complement the hematopoietic profiling, we next examined nonhematopoietic, stem/progenitor-enriched compartments within the $CD45^-$ populations to determine how supramolecular composition influences recruitment of regenerative stromal phenotypes. Flow cytometry quantification of aggregated stem cell markers (fig. S16) revealed that SLan-containing hydrogels—both SLan alone and the 1:1 SLan:K1 formulation—displayed significantly elevated levels of Sca-1^+ progenitor cells at both days 3 and 7, compared to the mechanically robust but bioinert K1 matrix. This enrichment was most prominent within the $CD45^-$/$CD11b^-$/Sca-1^+/$CD34^-$ compartments, a phenotype consistent with tissue-resident mesenchymal or mesenchymal-like stromal progenitors. The enhanced recruitment of these cells aligns with the robust endothelial infiltration (Fig. 4, A to E) and with the higher vessel densities visualized histologically in subcutaneous implants in rats as well (Fig. 5, H to K, and fig. S14), reinforcing the link between VEGFR2 accessibility, progenitor mobilization, and early angiogenic niche formation.

The 1:1 SLan:K1 hybrid scaffold reproducibly recapitulated the SLan phenotype, suggesting that coassembly preserves the ability of SLan to recruit reparative stromal subsets while benefiting from increased mechanical retention. This observation supports a vision that molecular partitioning of bioactive SLan within a K1-stabilized matrix allows for sustained presentation of pro-angiogenic cues, thereby enabling prolonged interactions with endogenous progenitor populations. In contrast, K1 alone recruited markedly fewer Sca-1^+ stromal cells, consistent with its lack of bioactive epitope and its comparatively slower engagement with proregenerative cell lineages.

To further dissect these trends, we analyzed disaggregated nonhematopoietic phenotypes (fig. S17), separating Sca-1^+ subsets, $CD105^+$ stromal progenitors, and $CD45^-$/$CD11b^+$ myeloid-like transitional cells. SLan and 1:1 hydrogels again showed an overrepresentation of Sca-1^+ stem/progenitor phenotypes, whereas K1 exhibited a relative increase in non–stem Sca-1^- stromal cells. Across all hydrogels, only minor differences were observed in the $CD45^-$/$CD11b^+$ myeloid-like fraction, and these did not reach statistical significance, indicating that the major effects of supramolecular composition manifest primarily within the stem/progenitor compartment rather than in non–stem stromal subsets.

Temporal comparison demonstrated that, similar to the hematopoietic profiles, the most pronounced differences occurred at day 3, with progressive convergence by day 7. This pattern implies that early progenitor recruitment is highly sensitive to the biochemical presentation and receptor-level accessibility of the scaffold, whereas later phases reflect a shared progression toward tissue remodeling once initial niche establishment has occurred. Together, these data suggest that SLan-driven bioactivity governs the early recruitment of regenerative stromal phenotypes, whereas the addition of K1 stabilizes the scaffold sufficiently to sustain these cues without diminishing their potency.

Overall, the integration of hematopoietic, endothelial, and stromal progenitor analyses reveals a coherent picture in which SLan-containing matrices rapidly generate a pro-angiogenic, proresolving cellular environment, whereas K1 biases toward early inflammatory clearance with reduced progenitor engagement. The 1:1 SLan:K1 coassembled hydrogel uniquely harmonizes these features, coupling SLan-like regenerative recruitment with enhanced mechanical persistence correlating with increased vessel density and lumenized structures observed histologically in rats (Fig. 5, H to K, and fig. S14) and mice (figs. S16 and S17) (*47*). These findings highlight the importance of supramolecular partitioning as a design principle for engineering synthetic scaffolds capable of orchestrating both immune resolution and angiogenic regeneration.

Collectively, these results indicate that coassembled scaffolds integrate mechanical durability with a pro-angiogenic and proresolving immune niche, recapitulating the efficacy of SLan while mitigating its rapid degradation. Together, the in vivo data establish that molecular partitioning between K1 and SLan preserves receptor-level bioactivity, promotes early endothelial recruitment, and guides innate immune resolution. The resulting angiogenic phenotype mirrors that of the pure SLan system but benefits from the enhanced retention and structural integrity conferred by K1. This synergy defines a tunable design principle for growth factor–free materials in which supramolecular composition dictates both vascular kinetics and immune remodeling at the implant-tissue interface.

In summary, this study provides the foundation for engineering around the barriers of self-assembly presented by bulky bioactive domains that may sterically hinder assembly and provides a framework for future research in combining multiple bioactive signals. The structure-function relationships, along with material tunability, may eventually allow for rationalized novel bioactive domain placement with an understanding of the trade-off between bioactivity and mechanical properties.

Coassembly rather than self-sorting in the SLan:K1 system is supported by three converging lines of evidence. First, solid-state ^{13}C CP/MAS NMR spectra (Fig. 2B) are uniform across all SLan:K1 ratios and closely mirror pure K1. MD simulations of randomly coassembled fibrils (Figs. 1B and 3, A to C) confirmed stable mixed–β sheet structures over microsecond timescales, and rheological properties scale continuously with SLan:K1 ratio (Fig. 1Q and fig. S5, O to R), inconsistent with the biphasic mechanical profile expected from two self-sorted fibril populations. This behavior is further supported

by recent works demonstrating that PAs sharing β sheet propensity and supramolecular chirality preferentially coassemble, consistent with both SLan and K1 sharing an identical $(SL)_6$ backbone (*48*). Although fluorescence resonance energy transfer (FRET) would provide additional direct evidence, fluorophore conjugation (400 to 600 Da) substantially reduces solubility of PAs and introduces steric hindrance in supramolecular assemblies (~1500 to 3000 Da); moreover, the observed degeneracy of the β sheet by NMR—indicative of register shifts across β sheet leaflets—raises reliability concerns for FRET-based measurements in this system.

Overall, by creating a stiffer matrix that preserves the bioactivity of the original molecule, we can both extend the localized effect of the peptide and provide a therapeutic niche that recruits and stimulates cells with the targeted receptors of our tunable design platform. Ideally, bioactivity and mechanical stiffness would be independent properties, but this investigation affords a previously unknown understanding of the nonintuitive trade-offs inherent with this system, wherein doping with nonfunctional components can preserve/enhance (on a per molar basis) signaling.

MATERIALS AND METHODS

Peptide synthesis and formulation

Peptides were manufactured in house using a CEM LibertyBlue automated peptide synthesizer (CEM, NC), using standard 9-fluorenyl methoxycarbonyl (Fmoc) solid-phase peptide synthesis chemistry with Rink Amide resin, *N*,*N*′-dimethylformamide (DMF) solvent, N-terminal acetylation using 10 vol % acetic anhydride in DMF, and trifluoracetic acid cleavage. Purity (>90%) was determined using high-performance liquid chromatography/electrospray ionization mass spectrometry (Agilent LC/QQQ); peptides were identically synthesized and purified by contract purchase from an API manufacturer (GenScript Inc., NJ). Lyophilized peptides were measured by weight and formulated in 1x phosphate-buffered saline (PBS) by sequentially solvating with 90% solvent volume Milli-Q H_2O and addition of 10% solvent volume of 10X PBS.

Bulk secondary structure determination

The secondary structure of the fibrils was determined using CD using an Olis RSM 1000 (OLIS Inc., Bangalore, India) spectrophotometer. Formulations were diluted 100X to 65.9 μM (equivalent to 0.01 wt % K1) in sequential 1:10 dilutions in Milli-Q water. A 350-μl diluted peptide hydrogel was added to a 0.1-cm light path/350-μl quartz cuvette (Alpha Nanotech, Vancouver, CA) (*30*, *32*). Runs from 190 to 240 nm were performed with a step size of 0.5 nm and an integration time of 1 s per step. The four runs were averaged for the raw spectra and smoothed using the smoothing filter algorithm on the Olis SpectralWorks software with a smoothing value of 17 arbitrary units.

Rheometric analysis

Shear rheology tests were performed using an HR-2 Discovery Hybrid Rheometer (TA Instruments, DE), equipped with a 40-mm-diameter parallel plate geometry. Approximately 300 μl of the peptide hydrogel at 6.59 mM (prepared as described in the section "Peptide synthesis and formulation") was placed on the sample stage (*13*). The upper plate was then lowered until the peptide hydrogel spread to fully cover the plate surface, yielding a gap distance of ~200 μm. Oscillatory strain sweeps were first conducted by applying shear strains from 0.01 to 100% at a constant frequency of 1 Hz; meanwhile, both the storage modulus and loss modulus were recorded. Frequency sweeps were then performed over a range of 0.01 to 100 Hz at a fixed strain amplitude of 1%, with the storage modulus and loss modulus measured at each frequency. All experiments were performed at room temperature (20°C). To minimize hydrogel drying, a TA Instruments DHR Solvent Trap was used throughout testing. On each peptide hydrogel, three repeated tests were conducted (*20*).

NMR analysis

NMR measurements were recorded on a 500-MHz Bruker spectrometer, with a 3.2-mm HCN MAS probe along with a 3.2-mm Bruker Low-E $^{1}H/^{13}C/^{15}N$ NMR probe. To calibrate, we measured the NMR signal of adamantane (*49*). We verified the ^{13}C chemical shift of adamantane relative to tetramethylsilane (TMS), which occurs at 38.38 and 29.45 ppm (*49*). One-dimensional (1D) ^{13}C CP/MAS experiments (*22*) were recorded at a MAS rate of 10 kHz. Subsequently recorded signals were averaged over a period of 15 hours.

Representation of fibrils

A TCL script was written to generate random assemblies of two-sheet SLan-K1 60-mers at different ratios, with an in-sheet distance of 9 Å and an intersheet distance of 5 Å, positioned to put the monomers as close as possible and to minimize steric overlaps. Fiber formation was then examined under three conditions. Monomer representations of SLan and K1 were generated by using PyMOL's fab command with secondary structures specified for the β sheet self-assembling domain and α-helical bioactive domain. The fibrils were assembled using either a PyMOL Python script (Supplementary Methods 2) or a VMD Perl script (Supplementary Methods 2) with a 5-Å lateral spacing between monomers and a 10-Å vertical spacing between monomers. To represent the random colocation of SLan and K1 monomers in the composite fibrils, we used an Excel random number generator for 60 positions, selecting the highest value numbers for the SLan position (*14*).

MD simulations of fibrils alone

In the first setup, preassembled 60-mers with varying ratios were equilibrated for 1 μs. In the second setup, 60 individual monomers at different ratios were equilibrated for 2 μs to monitor the self-assembly process over time. In the third setup, 60 individual monomers were introduced into a 1-μs-equilibrated assembly of 60-mers and further equilibrated for 500 ns to investigate the fiber growth process.

MD simulations

Atomistic MD simulations were performed using NAMD 3.0 (http://ks.uiuc.edu/Research/namd/) with the CHARMM36 protein force field and TIP3 water representation (*50*–*52*). All simulations were performed in a physiological solution with 0.15 M NaCl, using parameters described previously and in Supplemental Methods 2 (*14*).

Atomic force microscopy

AFM analysis was performed on 0.01 wt % formulations. The peptides were spin coated on freshly cleaved mica discs and then rinsed twice with Milli-Q water. Coated mica was allowed to dry for at minimum 30 min. Images were taken on a Bruker Dimension Icon AFM (Bruker, MA) using ScanAsyst mode in air using 512 samples per line with a 1-μm scan increment (*30*, *32*, *53*).

Transmission electron microscopy

Formulations were diluted to a final working concentration of 0.0659 mM in ultrapure water. Carbon/formvar 400 mesh, Cu Holey grids (Electron Microscopy Sciences, PA) were glow discharged and rendered hydrophilic on a Pelco Easiglow (Ted Pella, CA) at 15 mA for 1 min (0.39 mbar). Next, a 150-mm petri dish was covered with parafilm where 30 μl of the peptide was spotted on the plate. Grids were placed on the specimen and allowed to adsorb to the grid surface using the Drop-to-Drop method for 5 min. The excess peptide was wicked away with filter paper and transferred to a water spot for 10 s, followed by negative staining with a 1% (w/v) uranyl acetate solution for 2 min; excess water and stain were similarly wicked away with filter paper. Grids were transferred to a covered petri dish and allowed to dry overnight at room temp before imaging on a Tecnai-12 transmission electron microscope operating at 80 kV. Images were collected using a Gatan OneView CMOS camera.

Cryo–electron microscopy

Formulations were diluted to a concentration of 0.33 mM in PBS. The peptides were then mixed by combining equal volumes of each to make the 1:1 combination. The peptide solutions were then vortexed as described above. Three microliters of each sample was administered on glow-discharged holey copper-carbon or holey gold grids (Quantifoil Micro Tools GmbH) using a blot force of 3 on a VitroBot Mark IV System (Thermo Fisher Scientific). The gold grids were glow discharged for 1 min, and a 30-s wait time and 7-s blot time were used for the blotting procedure. For the carbon grids, a glow discharge time of 30 s, a wait time of 28 s, and a blot time of 5 s was prescribed. All grids were then rapidly submerged in liquid ethane for vitrification. Data were collected on a Tundra Cryo-TEM (Thermo Fisher Scientific) with an excitation voltage of 100 keV. All images collected had an approximate pixel scale of 0.0745 nm/pixel. Data were captured automatically in .mrc format. Images were uploaded to ImageJ, with raw images denoised using the "despeckle" filter and contrast enhancement functions. Scaling was performed on ImageJ using .xml file metadata for each captured image. Fibril lengths were measured with the median of 15 used to provide semi-quantitative analysis of comparative fibril lengths, noting that fibers may span the length of the image; fibers may pass through the plane of the image; and curvilinear nature may not be fully accounted for with 2D EM images.

Binding kinetics measurement

Recombinant His-tagged domains 1 to 7 of human VEGFR2 (ACROBiosystems, DE; catalog no. VE2-H5255) and human VEGF165 (VEGF-A isotype, catalog no. VE5-H5248; ACROBiosystems) were used. All coincubation and solvation steps were performed in Hepes-T buffer, consisting of 10 mM Hepes, 150 mM NaCl, and 0.05% Tween 20. We used a NanoTemper His-Tag labeling kit (Catalog no. MO-L018; NanoTemper Technologies, CA) and first assessed the disassociation constant between the target protein and the labeling dye. The protein was coincubated with a 100 mM dye at a concentration 20x the calculated disassociation constant of the dye and the protein. Serial dilutions (1:2) of the peptide in buffer were prepared, and the dyed protein solution was introduced at a 50:50 ratio (*21*, *54*). Spectral shift measurements were taken using a NanoTemper Monolith X (*55*).

Cell culture and protein lysate collection

Passage 4 to 5 HUVECs were seeded (5×10^4 per well) into flat-bottom 6-well tissue culture plates (Falcon, catalog no. 353046), supplemented with 2.5 ml of EGM-2 Endothelial Cell Growth Medium-2 BulletKit (Lonza, catalog no. CC-3162), and left to incubate for 72 hours before reaching 85 to 90% confluency. Each well was washed with 1 ml of 1X PBS before initiating a 2-hour serum starvation using supplement-free EGM-2 medium (i.e., BulletKit supplements were not added to basal medium). For groups administered axitinib in a conditioned medium, the inhibitor was added to respective groups during serum starvation at 10 μM. Next, the conditioned medium was formulated using supplement-free EGM-2 medium where the dimethyl sulfoxide (DMSO) (Fisher, catalog no. BP231-100), axitinib, and VEGF-A (ACROBiosystems, catalog no. VE5-H5248) groups were prepared at 10 μM, 1 μM, and 100 nM, respectively. Formulations were diluted to a final working concentration of 10 μM for each group's respective treatment condition. In addition, these groups were supplemented with 1 μM DMSO to account for any effects conferred by DMSO in the initial reconstitution of VEGF-A/axitinib. After the 2-hour serum starvation, each well was washed with 1X PBS before applying each respective treatment condition into their respective 6-well plate.

Following an incubation time of 10 min, the conditioned medium was aspirated, and wells were washed with ice-cold 1X PBS. Next, 100 μl of cell lysis buffer [radioimmunoprecipitation assay (RIPA) buffer: Pierce, catalog no. 89900; Phosphatase Inhibitor Cocktail (100X): Halt, catalog no. 78420; and Protease Inhibitor Cocktail: Sigma-Aldrich, catalog no. P8340] was prepared for each 6-well plate and added to the first well of each plate on ice and a cell scraper (VWR, catalog no. 10062-906) was used to spread lysis solution across the well before sequentially pipetting the lysate into the subsequent well where scraping and collection were repeated. Lysates were then sonicated for 1 min before centrifuging samples at 20,000*g* for 20 min at 4°C; the supernatant was transferred to a new tube for protein quantification using a BSA standard (Novagen, catalog no. 71285-3).

Secondary signaling measurements

To measure phosphoproteins in the MAPK pathway, a Multiplexed Luminex Immunoassay (Millipore, 48-660MAG) was used. The MAPK panel detected pATF2 (Thr^{71}), pErk (Thr^{185}/Tyr^{187}), pHSP27 (Ser^{78}), pJNK (Thr^{183}/Tyr^{185}), p-c-Jun (Ser^{73}), pMEK1 (Ser^{222}), pMSK1 (Ser^{212}), p38 (Thr^{180}/Tyr^{182}), p53 (Ser^{15}), and pSTAT1 (Tyr^{701}). Before analysis, lysates were thawed on ice and centrifuged at 4°C for 10 min at 13,000 rpm. Protein concentrations were normalized to 1 μg protein per sample per 6.25 μl using additional RIPA buffer as a diluent. The assay was read on an Intelliflex Instrument (Luminex) (*56*).

Animals implants

All the animal studies were performed in compliance and with approval from the University of Houston (protocol no. PROTO202500035) and the NJIT-Rutgers (protocol no. PROTO201900023) Institutional Animal Care and Use Committee (IACUC) guidelines. C57BL/6 mice (6 to 8 weeks old) or Wistar rats (9 to 10 weeks old) were purchased from Charles River Laboratories. Animals were allowed a minimum 1-week acclimatization period in a 12-hour light cycle with food and water provided ad libitum before the start of the study. Sterile prepared 6.59 mM hydrogels were mixed, centrifuged, and then aspirated into a 1-ml syringe. Animals were anesthetized

using isoflurane (3% for induction and 1% for maintenance) and shaved, and the administration site was sterile prepped using three alternating applications of isopropanol and povidone iodine solution. A 100-μl peptide hydrogel was injected into the subcutaneous space by pinching and lifting the administration site and injecting the peptide at a 45° angle with a 27-gauge needle for mice for fluorescence-activated cell sorting (FACS) and 200 μl in rats for subcutaneous evaluation. At the designated time points, the animals were euthanized by carbon dioxide asphyxiation. The bolus regions were immediately harvested, trimmed, and placed under ice-cold PBS.

Flow cytometry analysis

Harvested hydrogel boluses were trimmed and mechanically minced using surgical scissors and disposable scalpels, followed by chemical digestion with Liberase (0.2 Wünsch Units/ml) for 15 min at 37°C. Cell suspensions with 500,000 to 250,000 cells were counted using a hemocytometer and added to each tube and diluted 1:1 with FACS buffer [2% (v/v) heat-inactivated fetal bovine serum (FBS) in 1X PBS]. Samples were incubated for 5 min with 2 μl of anti-CD16/CD32 Fc block antibody (Mouse BD Fc Block, BD Biosciences) at 4°C. Samples were costained for 30 min on ice with standard panels of immunophenotyping antibodies. Then, cells were washed with 1 ml of FACS buffer, centrifuged at 260*g* for 6 min, and washed again with 1X PBS. Cells were resuspended in 500 μl of 1X PBS and stained with Blue live/dead fixable dead cell stain (Invitrogen) for 30 min on ice. Cells were washed one more time with 1X PBS, pelleted by centrifugation, and resuspended in 200 μl of 1X PBS. The cell suspension was filtered through a 35-μm strainer and fixed with 200 μl of 1% paraformaldehyde in 1X PBS [adapted from (*57*)]. For exploration of transitory/nontransitory endothelial cell subpopulations, FACS was performed with CD31 (PECAM-1), CD144 (VE-Cadherin), and CD309 (VEGFR2) and analyzed on a BD FACS Fortessa X-20 I (BD Biosciences). All secondary antibodies used for the flow cytometry was performed with CD31 (PECAM-1), CD144 (VE-Cadherin), and CD309 (VEGFR2) and analyzed on a BD FACS Fortessa X-20 I (BD Biosciences). All antibodies used for the flow cytometry analysis are described in tables S1 to S3. Gating logic is outlined in figs. S18 and S19. Data were analyzed using BD FACSDIVA v9 (De Novo, CA) and FlowJo v10.10.0 (Ashland, OR). For analysis, a cell-only unstained control and single-parameter compensation (UltraComp eBeads PLUS; Invitrogen, 01-333-42) were used to guide manual gating. For tSNE spatial analysis, nearly 5000 cells from the $CD45^+$ populations were downsampled and concatenated into a single .fcs file. Clustering was performed using the tSNE tool in FlowJo with the standard myeloid panel (fig. S19) under 1000 iterations, perplexity of 30, and 200 learning rate parameters.

Histological analysis

Untrimmed samples with surrounding subcutaneous tissue were fixed in 10% buffered formalin. The fixed samples were embedded in paraffin and sectioned to a width of 5 μm using a Leica RM2255 Motorized Microtome (Leica Biosystems). The sections were applied to glass slides, and hematoxylin and eosin or Masson's trichrome stains was applied to the slides thereafter (*30*). The sections were imaged on an inverted microscope (Echo Revolve). The slides were processed and scaled and bolus outlined using QuPath 0.5.1. The blood vessel's density was manually quantified in the region outlined.

Statistical analysis

Significance was determined using a one-way analysis of variance (ANOVA), calculated with the software as stated in the captions of the corresponding figures, unless otherwise noted in the caption of the corresponding figure. All data were checked for normality and variance consistency before proceeding to run the parametric test. The Tukey's pairwise comparisons were performed with *P* value corrections calculated using Prism 4.5.1. For flow cytometry, a Shapiro-Wilk test for normality and Levene's test for homogeneity of variance were used. For parametric tests, a regular one-way ANOVA was performed with post hoc Tukey's pairwise comparisons. When conditions of normality were violated, a Kruskal-Wallis test with post hoc two-sample Wilcoxon tests were used. For η^2 and ε^2 effect size values, ≥ 0.01 = small effect, ≥ 0.06 = moderate effect, and ≥ 0.14 = large effect. For Cohen's *d*, ≥ 0.2 = small effect, ≥ 0.5 = moderate effect, and ≥ 0.8 = large effect. For Cliff's δ, ≥ 0.147 = small effect, ≥ 0.33 = moderate effect, and ≥ 0.474 = large effect. Analyses were performed in RStudio version 4.3.1.

Supplementary Materials

This PDF file includes:

Figs. S1 to S19
Tables S1 to S4
Supplementary Methods 1 and 2
References

REFERENCES

1. B. R. Freedman, C. Hwang, S. Talbot, B. Hibler, S. Matoori, D. J. Mooney, Breakthrough treatments for accelerated wound healing. *Sci. Adv.* **9**, eade7007 (2023).
2. M. Chang, T. T. Nguyen, Strategy for treatment of infected diabetic foot ulcers. *Acc. Chem. Res.* **54**, 1080–1093 (2021).
3. N. Papanas, E. Maltezos, Becaplermin gel in the treatment of diabetic neuropathic foot ulcers. *Clin. Interv. Aging* **3**, 233–240 (2008).
4. Y. Xue, Y. Zhang, Y. Zhong, S. Du, X. Hou, W. Li, H. Li, S. Wang, C. Wang, J. Yan, D. D. Kang, B. Deng, D. W. McComb, D. J. Irvine, R. Weiss, Y. Dong, LNP-RNA-engineered adipose stem cells for accelerated diabetic wound healing. *Nat. Commun.* **15**, 739 (2024).
5. J. Hu, L. Zhang, C. Liechty, C. Zgheib, M. M. Hodges, K. W. Liechty, J. Xu, Long noncoding RNA GAS5 regulates macrophage polarization and diabetic wound healing. *J. Invest. Dermatol.* **140**, 1629–1638 (2020).
6. X. Li, N. Li, B. Li, Y. Feng, D. Zhou, G. Chen, Noncoding RNAs and RNA-binding proteins in diabetic wound healing. *Bioorg. Med. Chem. Lett.* **50**, 128311 (2021).
7. Y. Zhang, Y.-Y. Zhang, Z.-W. Pan, Q.-Q. Li, L.-H. Sun, X. Li, M.-Y. Gong, X.-W. Yang, Y.-Y. Wang, H.-D. Li, L.-N. Xuan, Y.-C. Shao, M.-M. Li, M.-Y. Zhang, Q. Yu, Z. Li, X.-F. Zhang, D.-H. Liu, Y.-M. Zhu, Z.-Y. Tan, Y.-Y. Zhang, Y.-Q. Liu, Y. Zhang, L. Jiao, B.-F. Yang, GDF11 promotes wound healing in diabetic mice via stimulating HIF-1α-VEGF/SDF-1α-mediated endothelial progenitor cell mobilization and neovascularization. *Acta Pharmacol. Sin.* **44**, 999–1013 (2023).
8. V. A. Kumar, N. L. Taylor, S. Shi, B. K. Wang, A. A. Jalan, M. K. Kang, N. C. Wickremasinghe, J. D. Hartgerink, Highly angiogenic peptide nanofibers. *ACS Nano* **9**, 860–868 (2015).
9. L. D. D'Andrea, G. Iaccarino, R. Fattorusso, D. Sorriento, C. Carannante, D. Capasso, B. Trimarco, C. Pedone, Targeting angiogenesis: Structural characterization and biological properties of a de novo engineered VEGF mimicking peptide. *Proc. Natl. Acad. Sci. U.S.A.* **102**, 14215–14220 (2005).
10. V. A. Kumar, Q. Liu, N. C. Wickremasinghe, S. Shi, T. T. Cornwright, Y. Deng, A. Azares, A. N. Moore, A. M. Acevedo-Jake, N. R. Agudo, S. Pan, D. G. Woodside, P. Vanderslice, J. T. Willerson, R. A. Dixon, J. D. Hartgerink, Treatment of hind limb ischemia using angiogenic peptide nanofibers. *Biomaterials* **98**, 113–119 (2016).
11. K. M. Galler, L. Aulisa, K. R. Regan, R. N. D'Souza, J. D. Hartgerink, Self-assembling multidomain peptide hydrogels: Designed susceptibility to enzymatic cleavage allows enhanced cell migration and spreading. *J. Am. Chem. Soc.* **132**, 3217–3223 (2010).
12. L. Aulisa, H. Dong, J. D. Hartgerink, Self-assembly of multidomain peptides: Sequence variation allows control over cross-linking and viscoelasticity. *Biomacromolecules* **10**, 2694–2698 (2009).
13. Z. Siddiqui, B. Sarkar, K. K. Kim, N. Kadincesme, R. Paul, A. Kumar, Y. Kobayashi, A. Roy, M. Choudhury, J. Yang, E. Shimizu, V. A. Kumar, Angiogenic hydrogels for dental pulp revascularization. *Acta Biomater.* **126**, 109–118 (2021).

14. J. Dodd-O, A. Roy, Z. Siddiqui, R. Jafari, F. Coppola, S. Ramasamy, A. Kolloli, D. Kumar, S. Kaundal, B. Zhao, R. Kumar, A. S. Robang, J. Li, A.-R. Azizogli, V. Pai, A. Acevedo-Jake, C. Heffernan, A. Lucas, A. C. McShan, A. K. Paravastu, B. V. V. Prasad, S. Subbian, P. Král, V. Kumar, Antiviral fibrils of self-assembled peptides with tunable compositions. *Nat. Commun.* **15**, 1142 (2024).
15. M. J. Webber, J. Tongers, C. J. Newcomb, K. T. Marquardt, J. Bauersachs, D. W. Losordo, S. I. Stupp, Supramolecular nanostructures that mimic VEGF as a strategy for ischemic tissue repair. *Proc. Natl. Acad. Sci. U.S.A.* **108**, 13438–13443 (2011).
16. A. N. Moore, T. L. Lopez Silva, N. C. Carrejo, C. A. Origel Marmolejo, I. C. Li, J. D. Hartgerink, Nanofibrous peptide hydrogel elicits angiogenesis and neurogenesis without drugs, proteins, or cells. *Biomaterials* **161**, 154–163 (2018).
17. L.-C. Huang, H.-C. Wang, L.-H. Chen, C.-Y. Ho, P.-H. Hsieh, M.-Y. Huang, H. C. Wu, T. W. Wang, Bioinspired self-assembling peptide hydrogel with proteoglycan-assisted growth factor delivery for therapeutic angiogenesis. *Theranostics* **9**, 7072–7087 (2019).
18. N. C. Wickremasinghe, V. A. Kumar, S. Shi, J. D. Hartgerink, Controlled angiogenesis in peptide nanofiber composite hydrogels. *ACS Biomater. Sci. Eng.* **1**, 845–854 (2015).
19. C. Han, Z. Zhang, J. Sun, K. Li, Y. Li, C. Ren, Q. Meng, J. Yang, Self-assembling peptide-based hydrogels in angiogenesis. *Int. J. Nanomedicine* **15**, 10257–10269 (2020).
20. A. S. Robang, A. Roy, J. B. Dodd-O, D. He, J. V. Le, A. C. McShan, Y. Hu, V. A. Kumar, A. K. Paravastu, Structural consequences of introducing bioactive domains to designer β-sheet peptide self-assemblies. *Biomacromolecules* **25**, 1429–1438 (2024).
21. A. Roy, J. B. Dodd-O, A. S. Robang, D. He, O. West, Z. Siddiqui, E. D. Aguas, H. Goldberg, A. Griffith, C. Heffernan, Y. Hu, A. K. Paravastu, V. A. Kumar, Self-assembling peptides with insulin-like growth factor mimicry. *ACS Appl. Mater. Interfaces* **16**, 364–375 (2024).
22. E. O. Stejskal, J. Schaefer, J. S. Waugh, Magic-angle spinning and polarization transfer in proton-enhanced NMR. *J. Magn. Reson.* **28**, 105–112 (1977).
23. P. R. Romero, N. Kobayashi, J. R. Wedell, K. Baskaran, T. Iwata, M. Yokochi, D. Maziuk, H. Yao, T. Fujiwara, G. Kurusu, E. L. Ulrich, J. C. Hoch, J. L. Markley, BioMagResBank (BMRB) as a resource for structural biology. *Methods Mol. Biol.* **2112**, 187–218 (2020).
24. D. S. Wishart, B. D. Sykes, F. M. Richards, The chemical shift index: A fast and simple method for the assignment of protein secondary structure through NMR spectroscopy. *Biochemistry* **31**, 1647–1651 (1992).
25. V. Daebel, S. Chinnathambi, J. Biernat, M. Schwalbe, B. Habenstein, A. Loquet, E. Akoury, K. Tepper, H. Müller, M. Baldus, C. Griesinger, M. Zweckstetter, E. Mandelkow, V. Vijayan, A. Lange, β-Sheet core of tau paired helical filaments revealed by solid-state NMR. *J. Am. Chem. Soc.* **134**, 13982–13989 (2012).
26. G. T. Debelouchina, G. W. Platt, M. J. Bayro, S. E. Radford, R. G. Griffin, Magic angle spinning nmr analysis of β2-microglobulin amyloid fibrils in two distinct morphologies. *J. Am. Chem. Soc.* **132**, 10414–10423 (2010).
27. M. Sarker, S. Park, V. Kumar, C. H. Lee, Micro-thin hydrogel coating integrated in 3D printing for spatiotemporal delivery of bioactive small molecules. *Biofabrication* **17**, 015019 (2024).
28. B. Sarkar, X. Ma, A. Agas, Z. Siddiqui, P. Iglesias-Montoro, P. K. Nguyen, K. K. Kim, J. Haorah, V. A. Kumar, In vivo neuroprotective effect of a self-assembled peptide hydrogel. *Chem. Eng. J.* **408**, 127295 (2021).
29. V. Harbour, C. Casillas, Z. Siddiqui, B. Sarkar, S. Sanyal, P. Nguyen, K. K. Kim, A. Roy, P. Iglesias-Montoro, S. Patel, F. Podlaski, P. Tolias, W. Windsor, V. Kumar, Regulation of lipoprotein homeostasis by self-assembling peptides. *ACS Appl. Bio Mater.* **3**, 8978–8988 (2020).
30. P. K. Nguyen, B. Sarkar, Z. Siddiqui, M. McGowan, P. Iglesias-Montoro, S. Rachapudi, S. Kim, W. Gao, E. J. Lee, V. A. Kumar, Self-assembly of an antiangiogenic nanofibrous peptide hydrogel. *ACS Appl. Bio Mater.* **1**, 865–870 (2018).
31. K. K. Kim, Z. Siddiqui, M. Patel, B. Sarkar, V. A. Kumar, A self-assembled peptide hydrogel for cytokine sequestration. *J. Mater. Chem. B* **8**, 945–950 (2020).
32. B. Sarkar, Z. Siddiqui, P. K. Nguyen, N. Dube, W. Fu, S. Park, S. Jaisinghani, R. Paul, S. D. Kozuch, D. Deng, P. Iglesias-Montoro, M. Li, D. Sabatino, D. S. Perlin, W. Zhang, J. Mondal, V. A. Kumar, Membrane-disrupting nanofibrous peptide hydrogels. *ACS Biomater. Sci. Eng.* **5**, 4657–4670 (2019).
33. P. K. Nguyen, W. Gao, S. D. Patel, Z. Siddiqui, S. Weiner, E. Shimizu, B. Sarkar, V. A. Kumar, Self-assembly of a dentinogenic peptide hydrogel. *ACS Omega* **3**, 5980–5987 (2018).
34. K. Kim, Z. Siddiqui, A. M. Acevedo-Jake, A. Roy, M. Choudhury, J. Grasman, V. Kumar, Angiogenic hydrogels to accelerate early wound healing. *Macromol. Biosci.* **22**, e2200067 (2022).
35. B. Sarkar, P. K. Nguyen, W. Gao, A. Dondapati, Z. Siddiqui, V. A. Kumar, Angiogenic self-assembling peptide scaffolds for functional tissue regeneration. *Biomacromolecules* **19**, 3597–3611 (2018).
36. A. N. Moore, J. D. Hartgerink, Self-assembling multidomain peptide nanofibers for delivery of bioactive molecules and tissue regeneration. *Acc. Chem. Res.* **50**, 714–722 (2017).
37. Z. Álvarez, A. N. Kolberg-Edelbrock, I. R. Sasselli, J. A. Ortega, R. Qiu, Z. Syrgiannis, P. A. Mirau, F. Chen, S. M. Chin, S. Weigand, E. Kiskinis, S. I. Stupp, Bioactive scaffolds with enhanced supramolecular motion promote recovery from spinal cord injury. *Science* **374**, 848–856 (2021).
38. X. Ma, A. Agas, Z. Siddiqui, K. Kim, P. Iglesias-Montoro, J. Kalluru, V. Kumar, J. Haorah, Angiogenic peptide hydrogels for treatment of traumatic brain injury. *Bioact. Mater.* **5**, 124–132 (2020).
39. D. Grant, N. Wanner, M. Frimel, S. Erzurum, K. Asosingh, Comprehensive phenotyping of endothelial cells using flow cytometry 1: Murine. *Cytometry A* **99**, 251–256 (2021).
40. D. Toledo-Flores, A. Williamson, N. Schwarz, S. Fernando, C. Dimasi, T. A. Witt, T. M. Nguyen, A. S. Puranik, C. D. Chue, S. Delacroix, D. B. Spoon, C. S. Bonder, C. A. Bursill, B. A. Di Bartolo, S. J. Nicholls, R. D. Simari, P. J. Psaltis, Vasculogenic properties of adventitial Sca-1^{+}CD45^{+} progenitor cells in mice: A potential source of vasa vasorum in atherosclerosis. *Sci. Rep.* **9**, 7286 (2019).
41. T. L. Lopez-Silva, C. F. Anderson, J. P. Schneider, Modulating neutrophil extracellular trap formation in vivo with locoregional precision using differently charged self-assembled hydrogels. *ACS Cent. Sci.* **11**, 465–478 (2025).
42. A. Hernandez, J. D. Hartgerink, S. Young, Self-assembling peptides as immunomodulatory biomaterials. *Front. Bioeng. Biotechnol.* **11**, 1139782 (2023).
43. M. A. Fernandez-Yague, L. A. Hymel, C. E. Olingy, C. McClain, M. E. Ogle, J. R. García, D. Minshew, S. Vyshnya, H. S. Lim, P. Qiu, A. J. García, E. A. Botchwey, Analyzing immune response to engineered hydrogels by hierarchical clustering of inflammatory cell subsets. *Sci. Adv.* **8**, eabd8056 (2022).
44. F. Veglia, E. Sanseviero, D. I. Gabrilovich, Myeloid-derived suppressor cells in the era of increasing myeloid cell diversity. *Nat. Rev. Immunol.* **21**, 485–498 (2021).
45. V. Bronte, S. Brandau, S. H. Chen, M. P. Colombo, A. B. Frey, T. F. Greten, S. Mandruzzato, P. J. Murray, A. Ochoa, S. Ostrand-Rosenberg, P. C. Rodriguez, A. Sica, V. Umansky, R. H. Vonderheide, D. I. Gabrilovich, Recommendations for myeloid-derived suppressor cell nomenclature and characterization standards. *Nat. Commun.* **7**, 12150 (2016).
46. B. H. Pogostin, M. H. Yu, A. R. Azares, E. M. Euliano, C. S. E. Lai, G. Saenz, S. X. Wu, A. C. Farsheed, S. M. Melhorn, T. P. Graf, D. G. Woodside, J. D. Hartgerink, K. J. McHugh, Multidomain peptide hydrogel adjuvants elicit strong bias towards humoral immunity. *Biomater. Sci.* **10**, 6217–6229 (2022).
47. A. Cossarizza, H.-D. Chang, A. Radbruch, S. Abrignani, R. Addo, M. Akdis, I. Andrä, F. Andreata, F. Annunziato, E. Arranz, P. Bacher, S. Bari, V. Barnaba, J. Barros-Martins, D. Baumjohann, C. G. Beccaria, D. Bernardo, D. A. Boardman, J. Borger, C. Böttcher, L. Brockmann, M. Burns, D. H. Busch, G. Cameron, I. Cammarata, A. Cassotta, Y. Chang, F. G. Chirdo, E. Christakou, L. Čičin-Šain, L. Cook, A. J. Corbett, R. Cornelis, L. Cosmi, M. S. Davey, S. De Biasi, G. De Simone, G. D. Zotto, M. Delacher, F. D. Rosa, J. D. Santo, A. Diefenbach, J. Dong, T. Dörner, R. J. Dress, C.-A. Dutertre, S. B. G. Eckle, P. Eede, M. Evrard, C. S. Falk, M. Feuerer, S. Fillatreau, A. Fiz-Lopez, M. Follo, G. A. Foulds, J. Fröbel, N. Gagliani, G. Galletti, A. Gangaev, N. Garbi, J. A. Garrote, J. Geginat, N. A. Gherardin, L. Gibellini, F. Ginhoux, D. I. Godfrey, P. Gruarin, C. Haftmann, L. Hansmann, C. M. Harpur, A. C. Hayday, G. Heine, D. C. Hernández, M. Herrmann, O. Hoelsken, Q. Huang, S. Huber, J. E. Huber, J. Huehn, M. Hundemer, W. Y. K. Hwang, M. Iannacone, S. M. Ivison, H.-M. Jäck, P. K. Jani, B. Keller, N. Kessler, S. Ketelaars, L. Knop, J. Knopf, H.-F. Koay, K. Kobow, K. Kriegsmann, H. Kristyanto, A. Krueger, J. F. Kuehne, H. Kunze-Schumacher, P. Kvistborg, I. Kwok, D. Latorre, D. Lenz, M. K. Levings, A. C. Lino, F. Liotta, H. M. Long, E. Lugli, K. N. M. Donald, L. Maggi, M. K. Maini, F. Mair, C. Manta, R. A. Manz, M.-F. Mashreghi, A. Mazzoni, J. M. Cluskey, H. E. Mei, F. Melchers, S. Melzer, D. Mielenz, L. Monin, L. Moretta, G. Multhoff, L. E. Muñoz, M. Muñoz-Ruiz, F. Muscate, A. Natalini, K. Neumann, L. G. Ng, A. Niedobitek, J. Niemz, L. N. Almeida, S. Notarbartolo, L. Ostendorf, L. J. Pallett, A. A. Patel, G. I. Percin, G. Peruzzi, M. Pinti, A. G. Pockley, K. Pracht, I. Prinz, I. Pujol-Autonell, N. Pulvirenti, L. Quatrini, K. M. Quinn, H. Radbruch, H. Rhys, M. B. Rodrigo, C. Romagnani, C. Saggau, S. Sakaguchi, F. Sallusto, L. Sanderink, I. Sandrock, C. Schauer, A. Scheffold, H. U. Scherer, M. Schiemann, F. A. Schildberg, K. Schober, J. Schoen, W. Schuh, T. Schüler, A. R. Schulz, S. Schulz, J. Schulze, S. Simonetti, J. Singh, K. M. Sitnik, R. Stark, S. Starossom, C. Stehle, F. Szelinski, L. Tan, A. Tarnok, J. Tornack, T. I. M. Tree, J. J. P. van Beek, W. van de Veen, K. van Gisbergen, C. Vasco, N. A. Verheyden, A. von Borstel, K. A. Ward-Hartstonge, K. Warnatz, C. Waskow, A. Wiedemann, A. Wilharm, J. Wing, O. Wirz, J. Wittner, J. H. M. Yang, J. Yang, Guidelines for the use of flow cytometry and cell sorting in immunological studies (third edition). *Eur. J. Immunol.* **51**, 2708–3145 (2021).
48. M. H. Sangji, S. R. Lee, H. Sai, S. Weigand, L. C. Palmer, S. I. Stupp, Self-sorting vs coassembly in peptide amphiphile supramolecular nanostructures. *ACS Nano* **18**, 15878–15887 (2024).
49. C. R. Morcombe, K. W. Zilm, Chemical shift referencing in MAS solid state NMR. *J. Magn. Reson.* **162**, 479–486 (2003).
50. J. Huang, A. D. MacKerell Jr., CHARMM36 all-atom additive protein force field: Validation based on comparison to NMR data. *J. Comput. Chem.* **34**, 2135–2145 (2013).
51. K. Vanommeslaeghe, E. Hatcher, C. Acharya, S. Kundu, S. Zhong, J. Shim, E. Darian, O. Guvench, P. Lopes, I. Vorobyov, A. D. Mackerell Jr., CHARMM general force field: A force field for drug-like molecules compatible with the CHARMM all-atom additive biological force fields. *J. Comput. Chem.* **31**, 671–690 (2010).

52. J. C. Phillips, D. J. Hardy, J. D. C. Maia, J. E. Stone, J. V. Ribeiro, R. C. Bernardi, R. Buch, G. Fiorin, J. Hénin, W. Jiang, R. McGreevy, M. C. R. Melo, B. K. Radak, R. D. Skeel, A. Singharoy, Y. Wang, B. Roux, A. Aksimentiev, Z. Luthey-Schulten, L. V. Kalé, K. Schulten, C. Chipot, E. Tajkhorshid, Scalable molecular dynamics on CPU and GPU architectures with NAMD. *J. Chem. Phys.* **153**, 044130 (2020).
53. K. M. Crowe, Z. Siddiqui, V. Harbour, K. Kim, S. Syed, R. Paul, A. Roy, R. Naik, K. Mitchell, A. Mahajan, B. Sarkar, V. A. Kumar, Evaluation of injectable naloxone-releasing hydrogels. *ACS Appl. Bio Mater.* **3**, 7858–7864 (2020).
54. M. Jerabek-Willemsen, C. J. Wienken, D. Braun, P. Baaske, S. Duhr, Molecular interaction studies using microscale thermophoresis. *Assay Drug Dev. Technol.* **9**, 342–353 (2011).
55. A. Langer, T. Bartoschik, O. Cehlar, S. Duhr, P. Baaske, W. Streicher, A new spectral shift-based method to characterize molecular interactions. *Assay Drug Dev. Technol.* **20**, 83–94 (2022).
56. M. J. Chen, S. Ramesha, L. D. Weinstock, T. Gao, L. Ping, H. Xiao, E. B. Dammer, D. D. Duong, A. I. Levey, J. J. Lah, N. T. Seyfried, L. B. Wood, S. Rangaraju, Extracellular signal-regulated kinase regulates microglial immune responses in Alzheimer's disease. *J. Neurosci. Res.* **99**, 1704–1721 (2021).
57. T. L. Lopez-Silva, D. G. Leach, A. Azares, I. C. Li, D. G. Woodside, J. D. Hartgerink, Chemical functionality of multidomain peptide hydrogels governs early host immune response. *Biomaterials* **231**, 119667 (2020).
58. T. Darden, D. York, L. Pedersen, Particle mesh Ewald: An N·log(N) method for Ewald sums in large systems. *J. Chem. Phys.* **98**, 10089–10092 (1993).
59. Y. Han, P. Král, Computational design of ACE2-based peptide inhibitors of SARS-CoV-2. *ACS Nano* **14**, 5143–5147 (2020).
60. F. Coppola, T. Pavlíček, P. Král, Coupling of SARS-CoV-2 to Aβ amyloid fibrils. *ACS Omega* **9**, 9295–9299 (2024).
61. A. R. Azizogli, V. Pai, F. Coppola, R. Jafari, J. B. Dodd-O, R. Harish, B. Balasubramanian, J. Kashyap, A. M. Acevedo-Jake, P. Král, V. A. Kumar, Scalable inhibitors of the Nsp3-Nsp4 coupling in SARS-CoV-2. *ACS Omega* **8**, 5349–5360 (2023).

Acknowledgments: We thank A. Soliman and V. Salazar for independently reviewing the slides for vessel quantification under the direction of A.R. NAMD was developed by the Theoretical and Computational Biophysics Group in the Beckman Institute for Advanced Science and Technology at the University of Illinois at Urbana-Champaign. We acknowledge the use of instruments at the NMR Center at the Georgia Institute of Technology. We acknowledge access to the Laboratory for Advanced Imaging of the Rutgers–Newark, Department of Biological Sciences. We acknowledge access to the Rutgers Public Health Research Institute Cryo-Electron Microscopy Core Facility and thank A. Wei and V. Petrou for support in obtaining the images. **Funding:** This work was supported by the National Institute Health (NIDCR R01DE031812, NIA/NIMHH RF1AG073434-01A1, OD S10OD026875-01A1). P.K. acknowledges the support from NSF DMR 2212123. The content is solely the responsibility of the authors and does not necessarily represent the official views of the National Institutes of Health or National Science Foundation. This work as also supported in part by the Woodruff Faculty Fellowship at Georgia Tech. **Author contributions:** Authors' contributions are attributed on the basis of CRediT author statement. J.D.: Conceptualization, data curation, formal analysis, investigation, methodology, project administration, software, validation, visualization, writing—original draft, and writing—review and editing. B.S.: Conceptualization, data curation, formal analysis, investigation, methodology, project administration, resources, supervision, validation, visualization, writing—original draft, and writing—review and editing. A.R.: Data curation, formal analysis, investigation, methodology, project administration, supervision, validation, visualization, writing—original draft, and writing—review and editing. R.J.: Conceptualization, data curation, formal analysis, investigation, methodology, software, validation, visualization, writing—original draft, and writing—review and editing. T.R.S.: Investigation and visualization. A.H.: Formal analysis, investigation, visualization, writing—original draft, and writing—review and editing. D.H.: Formal analysis, investigation, and writing—review and editing. F.C.: Data curation, formal analysis, investigation, software, validation, visualization, writing—original draft, and writing—review and editing. D.M.D.: Data curation, formal analysis, investigation, software, validation, visualization, writing—original draft, and writing—review and editing. D.M.: Investigation and writing—review and editing. G.G.: Formal analysis and investigation. A.G.: Investigation and writing—review and editing. H.R.-W.: Data curation, investigation, visualization, writing—original draft, and writing—review and editing. S.P.: Data curation, investigation, visualization, writing—original draft, and writing—review and editing. E.B.: Data curation, formal analysis, investigation, methodology, project administration, resources, validation, and writing—review and editing. Y.H.: Data curation, formal analysis, investigation, and methodology. L.W.: Conceptualization, formal analysis, methodology, resources, supervision, visualization, and writing—review and editing. A.K.P.: Conceptualization, data curation, funding acquisition, investigation, methodology, project administration, resources, software, supervision, validation, visualization, writing—original draft, and writing—review and editing. P.K.: Conceptualization, data curation, formal analysis, funding acquisition, investigation, methodology, project administration, resources, software, supervision, validation, visualization, writing—original draft, and writing—review and editing. V.A.K.: Conceptualization, data curation, formal analysis, funding acquisition, investigation, methodology, project administration, resources, software, supervision, validation, visualization, writing—original draft, and writing—review and editing. **Competing interests:** The authors declare that they have no competing interests. **Data, code, and materials availability:** All data, materials, and code needed to evaluate and reproduce the results in the paper are present in the paper and/or the Supplementary Materials. Scripts for fibrils are available in the following Zenodo repository: https://doi.org/10.5281/zenodo.19742094. Materials/samples used in the analysis will be made available to any researcher for purposes of directly replicating the procedure upon reasonable request to V.A.K. (vkumar24@cougarnet.uh.edu).

Submitted 14 January 2026
Accepted 26 June 2026
Published 31 July 2026
10.1126/sciadv.aef5064

ScienceAdvances

Programming angiogenesis with tunable assemblies of multifunctional peptides

Joseph Dodd-o, Bobak Shadpoor, Abhishek Roy, Roya Jafari, Tarunya R. Sudarshan, Abigail Holberton, Dongjing He, Francesco Coppola, Daniel M. Dinakarapandian, Deep Malu, Gelavizh Gharati, Alexandra Griffith, Harrison Rohe-Weiner, Siya Patel, Edward Bonder, Yuhang Hu, Levi Wood, Anant K. Paravastu, Petr Kral, and Vivek A. Kumar

Sci. Adv. **12** (31), eaef5064. DOI: 10.1126/sciadv.aef5064